



This is a repository copy of *Use of three-terminal impedance spectroscopy to characterize sodium-ion batteries at various stages of cycle life.*

White Rose Research Online URL for this paper:

<https://eprints.whiterose.ac.uk/208397/>

Version: Published Version

Article:

Middlemiss, L.A. orcid.org/0000-0002-7840-4393, Rennie, A.J.R., Sayers, R. et al. (1 more author) (2024) Use of three-terminal impedance spectroscopy to characterize sodium-ion batteries at various stages of cycle life. *Journal of The Electrochemical Society*, 171 (1). 010528. ISSN 0013-4651

<https://doi.org/10.1149/1945-7111/ad1c0f>

Reuse

This article is distributed under the terms of the Creative Commons Attribution (CC BY) licence. This licence allows you to distribute, remix, tweak, and build upon the work, even commercially, as long as you credit the authors for the original work. More information and the full terms of the licence here:

<https://creativecommons.org/licenses/>

Takedown

If you consider content in White Rose Research Online to be in breach of UK law, please notify us by emailing eprints@whiterose.ac.uk including the URL of the record and the reason for the withdrawal request.



eprints@whiterose.ac.uk
<https://eprints.whiterose.ac.uk/>

OPEN ACCESS

Use of Three-Terminal Impedance Spectroscopy to Characterize Sodium-Ion Batteries at Various Stages of Cycle Life

To cite this article: Laurence A. Middlemiss *et al* 2024 *J. Electrochem. Soc.* **171** 010528

View the [article online](#) for updates and enhancements.

You may also like

- [Review—Advanced Secondary Batteries with Multi-Electron Reaction of Light Elements](#)

Tuo Zhao and Meiling Wang

- [Review—Current Collectors for Rechargeable Batteries: State-of-the-Art Design and Development Strategies for Commercial Products](#)

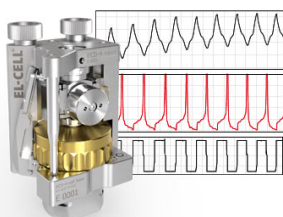
Pappu Naskar, Ankita Saha, Biplab Biswas *et al.*

- [Local Reaction Environment Deviations within Gas Diffusion Electrode Pores for CO₂ Electrolysis](#)

Esaar N. Butt, Johan T. Padding and Remco Hartkamp

Measure the Electrode Expansion in the Nanometer Range. Discover the new ECD-4-nano!


electrochemical test equipment



- Battery Test Cell for Dilatometric Analysis (Expansion of Electrodes)
- Capacitive Displacement Sensor (Range 250 μm , Resolution ≤ 5 nm)
- Detect Thickness Changes of the Individual Electrode or the Full Cell.

www.el-cell.com +49 40 79012-734 sales@el-cell.com





Use of Three-Terminal Impedance Spectroscopy to Characterize Sodium-Ion Batteries at Various Stages of Cycle Life

Laurence A. Middlemiss,¹ Anthony J. R. Rennie,² Ruth Sayers,² and Anthony R. West^{1,z}

¹Department of Materials Science and Engineering, The University of Sheffield, Sheffield S1 3JD, United Kingdom

²Faradion Ltd, The Innovation Centre, Sheffield S1 4DP, United Kingdom

The use of 3-terminal measurements to separate different impedance components of a prototype sodium-ion battery is outlined. By addition of a sodium metal reference electrode, the two electrode-electrolyte interfaces can be measured separately and changes monitored at various stages of battery cycle life. The impedance of a freshly-constructed cell is dominated by the blocking capacitance of the anode-electrolyte interface and the charge-transfer resistance at the cathode-electrolyte interface. The variation of these components during charge and discharge cycling provide a method to monitor evolution of cell performance.

© 2024 The Author(s). Published on behalf of The Electrochemical Society by IOP Publishing Limited. This is an open access article distributed under the terms of the Creative Commons Attribution 4.0 License (<http://creativecommons.org/licenses/by/4.0/>), which permits unrestricted reuse of the work in any medium, provided the original work is properly cited. [DOI: 10.1149/1945-7111/ad1c0f]



Manuscript submitted October 12, 2023; revised manuscript received December 11, 2023. Published January 24, 2024.

Supplementary material for this article is available [online](#)

Concerns surrounding the long-term sustainability, cost and safety of lithium-ion (Li-ion) batteries, have led researchers to seek alternative battery chemistries.¹ Of the “beyond lithium” technologies looked at to-date, sodium-ion (Na-ion) batteries have received the most interest and development.² Na-ion batteries, in contrast to Li-ion, can be made from abundant materials and are less susceptible to dangerous overheating.³ Layered sodium transition metal oxides, containing multiple metallic elements in addition to sodium, have shown the most potential for Na-ion cathode materials so far; these have easy-to-synthesise, simple structures, which are capable of high redox potentials and specific capacities.⁴

All batteries experience a reduction in performance during storage as well as cycling.⁵ This can be due to a variety of degradation (ageing) mechanisms, which can be associated with one or more of the components/interfaces of a cell. Degradation leads to decrease in (energy) capacity and/or power.⁶ The ability to maintain a high capacity over time, i.e. battery cycle life, is a key performance criterion with respect to the widespread commercialisation of Na-ion technology. Hence, knowledge of performance degradation and capacity fade is essential to fully characterise batteries and optimise their performance. Identification of problem interfaces and rate-limiting steps inside cells is of the utmost importance, so that these can be fully characterised and overcome. Extensive research has taken place over the past few decades into the causes and effects of Li-ion battery ageing,^{5,7} but relatively few similar studies into degradation of Na-ion cells have been reported, despite it being imperative to commercialisation of the technology.

Impedance spectroscopy (IS), also commonly referred to as electrochemical impedance spectroscopy (EIS), is a non-destructive technique which provides much information in a relatively short space of time, while preserving cell integrity.⁸ It allows in operando measurements during battery cycling as well as ex operando measurements at various states of charge (SoC) and discharge (SoD). Measurements take place across a wide frequency range which enables the separation of different components and processes that operate on different timescales. IS is particularly sensitive to systems that contain several series-connected impedance elements such as bulk components and interfaces, which makes it well-suited to study a multi-component device such as a battery. Although interpretation of IS results is not always straightforward, data analysis may be aided through the use of model equivalent electrical circuits;⁹ these help to assign different parts of the obtained impedance spectrum to circuit parameters which can then be related to different components and processes inside a sample or

electrochemical cell. IS has been used extensively in the past on Pb-acid and Li-ion batteries.^{10–12}

A major limitation in analysing conventional two-terminal EIS data is that it can be difficult to deconvolute impedance components from different regions of a battery that have similar time constants. Half-cell measurements can be used to study separately the impedances associated with the two electrode-electrolyte interfaces but may not reflect the processes occurring in a full-cell battery at different states of charge.¹³ Assembling a range of cell configurations in order to focus on impedance contributions from different components of a battery, such as symmetric^{14,15} and three-electrode¹⁶ arrangements, has been found to aid analysis. The study of symmetric cells is limited because they are unable to charge and discharge in the same way as a fully functioning battery.

The arduous process of disassembling and reassembling operational batteries for ex situ measurements must be carried out repeatedly, in order to gather information at different states of charge and health. However, the process of disassembling and reassembling cells may introduce additional artefacts/impedances that affect the validity of collected results.¹⁷ One way to circumvent the limitations of conventional two-electrode and symmetric cell EIS studies is by using a three-electrode setup that incorporates a spectator reference electrode which does not interfere with the battery cycling.¹³ The battery is charged/discharged as usual, but as well as recording the impedance across the entire cell, the impedances of the cathode and anode are measured separately against the reference. It is then possible to monitor how each electrode contributes to the overall impedance of the battery.¹⁸

A number of three-electrode studies have successfully identified the rate-limiting electrode/process inside different Li-ion batteries.^{16,19,20} Several three-terminal setups are reported in the literature, including modified commercial cells,²¹ as well as novel in-house designs.²² However, their usefulness is often curtailed by electrochemical/geometrical asymmetry in the design,²³ combined with a failure to check the validity of the setup.²⁴

Impedance spectroscopy is relatively easy to use experimentally, but difficulties can arise in interpretation of the results. Previous studies in the literature have rarely utilised the full range of impedance formalisms which implicitly apply different weightings to the data and facilitate deconvolution of complex data sets into impedance components, thus constraining their usefulness. An experimental set of impedance, Z^* data consists of resistive and reactive components. The resistance is often a combination of electronic and ionic resistances. Standard practice in data analysis is to present data as a Z^* complex plane plot of Z'' against Z' on linear scales, also known as a Nyquist plot, since this represents a good method to separate series-connected impedances. The

^zE-mail: a.r.west@sheffield.ac.uk

appropriate equivalent circuit is usually a series combination of the parallel RC elements, each of which represents different phenomena/interfaces whose time constants can be separated on the frequency scale. The disadvantage is that impedance data are weighted according to the resistance of the components and small resistances can easily be obscured by the presence of much larger resistances.

There are four commonly-used, inter-related formalisms for presenting impedance data:^{25,26}

Impedance, Z^*

$$\text{Admittance, } Y^* = [Z^*]^{-1} \quad [1]$$

$$\text{Electric modulus, } M^* = j\omega C_0 Z^* \quad [2]$$

$$\text{Permittivity, } \epsilon^* = [M^*]^{-1} = [j\omega C_0 Z^*]^{-1} = [j\omega C_0]^{-1} Y^* \quad [3]$$

For each, complex plane representations can be used as well as spectroscopic plots of real or imaginary components against frequency (also known as Bode plots). All formalisms use the same basic data sets but apply different weighting factors to the data which together, enable a more complete separation of the different components, especially in visual data presentations. It is not necessary to plot data in all formalisms and experience shows how, depending on the nature of the materials under study, certain presentations give insights that may not be apparent from Z^* plots alone. Particularly useful presentations are spectroscopic plots on logarithmic scales of the real part of the permittivity, ϵ' , since these plots separate regions according to their capacitance, C' because C' is related to the geometry (thickness, d and area, A) and permittivity of a region by:

$$C' = \epsilon_0 \epsilon' d/A \quad [4]$$

where ϵ_0 is the permittivity of free space. Usually, the intrinsic permittivity of a material is fairly small and temperature-independent, unless it is ferroelectric and in the vicinity of the Curie temperature, T_c . Component thicknesses can vary from millimetre dimensions for a bulk sample to interatomic distances for sample-electrode interfaces. Consequently, C' is controlled mainly by geometric factors and its values span several decades of frequency ranging from picoFarads to microFarads. In cases where significant electrochemical reactions occur on the timescale of the impedance measurements, capacitances in the milliFarad range may be obtained. Experimentally, $\log C'/\log f$ plots readily span up to 9 decades of both capacitance and frequency and give a visual representation of the make-up of a cell or material.

Impedance spectroscopy has been used to probe the performance-limiting factors in lithium-ion batteries, but much less on “beyond lithium” technology.^{27–29} Few studies have investigated EIS on full-cell Na-ion batteries and none, apart from our preliminary studies,³⁰ used a pouch cell design and/or a three-electrode configuration. The objectives of the present work were to extend EIS measurements to layered oxide sodium-ion batteries, using a three-electrode design, at varying states of charge. The validity of the experimental setup was confirmed and data analysed using different impedance formalisms, to give more in-depth and comprehensive analysis of results.

Experimental

The cathode used was a mixed phase material of two polymorphs, $P2\text{-Na}_{0.667}[\text{Ni}_{0.300}\text{Mn}_{0.600}\text{Mg}_{0.033}\text{Ti}_{0.067}]\text{O}_2$ and $O3\text{-Na}[\text{Ni}_{0.333}\text{Mn}_{0.333}\text{Mg}_{0.167}\text{Ti}_{0.167}]\text{O}_2$ both with layered rock salt structures.³¹ The composite cathode consisted of $\text{Na}[\text{Ni},\text{Mn},\text{Mg},\text{Ti}]\text{O}_2$ active material mixed with polyvinylidene fluoride (PVDF) binder and C65 carbon black conductive additive in a 89:6:5 ratio. The anode was a non-graphitisable carbon mixed with PVDF and C45 carbon black (88.1:9:2.9). Slurries were formed with N-methyl-2-pyrrolidone

(NMP), drawn down onto carbon-coated Al foil, dried and stored at 60 °C in a vacuum oven. Square electrodes were pressed using a die cutting machine. The electrodes were stored in a vacuum oven at 60 °C before transferring to an argon-filled glove box (Mbraun, $\text{H}_2\text{O} < 0.1$ ppm and $\text{O}_2 < 0.1$ ppm) for cell assembly.

The separators used to isolate cathode and anode were cut from GF/A glass microfiber filter paper (Whatman) and dried at 200 °C for 16 h before transferring to the glove box. In-house laminate-type prismatic pouch cells (7×5 cm) containing Al current collector tabs (MTI) to connect electrodes to the battery tester were dried at 70 °C overnight. The electrolyte was a solution of 0.5 M sodium hexafluorophosphate in a mixed carbonate solvent; its resistance was measured separately using a BioLogic high temperature conductivity cell (HTCC). Cells were assembled in the glove box by first placing the anode active side up, followed by two separators on top. Both separators were soaked in liquid electrolyte. Finally, the cathode was placed on top of the separators, with the active side facing the anode. The entire electrode-separator stack was placed inside of a laminated pouch, and vacuum-sealed, with Al current collector tabs sticking out of the pouch for connection to the battery tester. The three-electrode cell design possessed longer separators (35×25 mm) to accommodate a third (reference) electrode sandwiched between the separators, placed above the cathode and anode, Fig. 1. This third electrode was a piece of Na metal (0.5×0.5 cm) enclosed inside a folded Al current collector tab.

Positive electrodes (cathodes) of 2.5 mAh cm^{-2} (20×20 mm) were cycled against negative hard carbon electrodes (22×22 mm). The overall capacity of each Na-ion cell was ~ 10 mAh. Electrochemical cycling and ac impedance measurements were performed using either a Maccor Series 4000 with a Solartron Modulab or a potentiostat with a parallel frequency response analyser (Solartron Pstat 1470E/FRA 1455 A). All cells were held at a constant temperature of 30 ± 0.5 °C. Impedance was measured by applying an ac potential between two electrodes and measuring the current between them. For three-electrode measurements, three impedance scans were performed simultaneously, using different methods for connecting the Solartron equipment to the electrodes. In the first, the cell impedance was measured without using the reference electrode. In the second, the impedance of the working electrode ($\text{Na}[\text{Ni},\text{Mg},\text{Mn},\text{Ti}]\text{O}_2$) was measured against the reference (Na metal) electrode. In the third, the counter electrode (hard carbon) was measured versus the reference electrode.

Each cell was left for 32 h at 30 °C prior to cycling to allow time to equilibrate. Impedance measurements with a potentiostatic signal amplitude of 10 mV (peak to peak) were made before initial cycling of the cell and after each charging/discharging step followed by four hours for equilibration. An additional one-hour hold on open circuit after the impedance measurements allowed the cell to return to a steady state. Repeat cells were built and tested to check the reproducibility of collected results. Analysis of data for these showed a close similarity between the cells. While there were slight changes in the absolute values between cells, the overall impedance profile and main trends were found to be the same.

ZView software (Scribner Associates Inc.) was used for impedance data analysis. A geometry correction was performed, which consisted of dividing the active charge-transfer area (4 cm^2) by the separation between the two electrodes (0.26 mm). The first objective was to find the most appropriate equivalent circuit to represent data sets; data were presented in various formats to gain visually an overview of the various impedance components. Two formats were found to be particularly appropriate: first, Z'' vs Z' complex plane plots to highlight the main resistive components but with the disadvantage that small additional resistances were effectively hidden; second, $\log C'$ vs $\log f$ plots which gave equal weighting across the frequency spectrum to the various capacitive elements. Resistance and capacitance values for the separate components were obtained from intercepts on the Z' axis and frequency-independent plateau C' values, respectively.

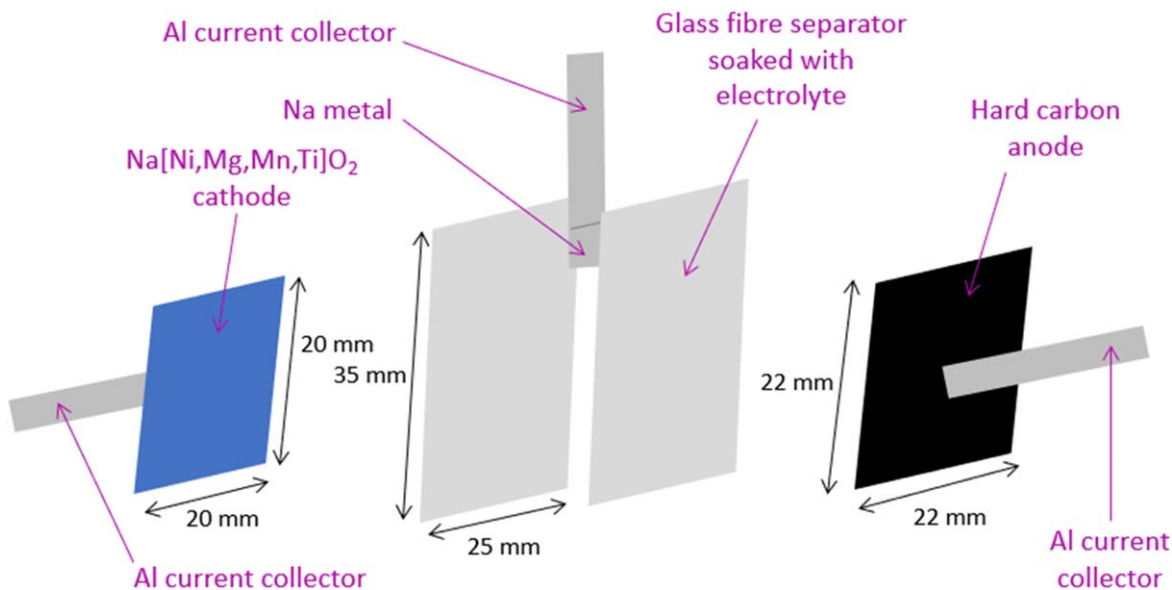


Figure 1. Three-electrode pouch cell design. The Na metal spectator reference electrode sits between the two separator layers, directly above the cathode/anode stack, in order to ensure accurate readings.

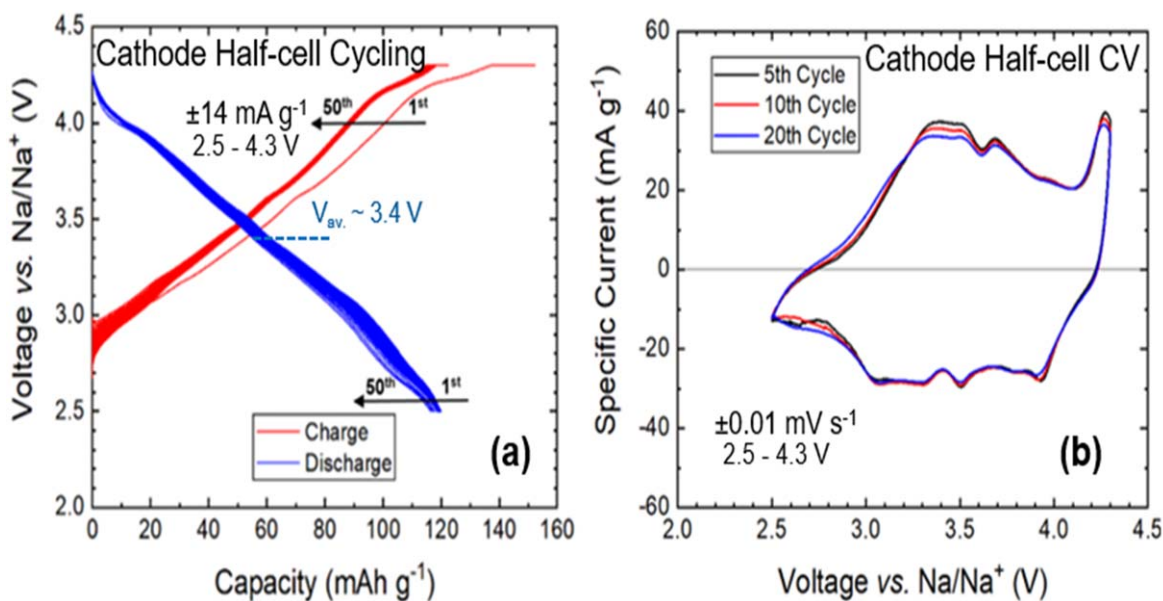


Figure 2. Overview of electrochemical properties of Na[Ni,Mg,Mn,Ti] O_2 layered oxide cathode material. (a) Half-cell (vs Na/Na $^+$) cycling at $\pm 14 \text{ mA g}^{-1}$, and (b) cyclic voltammetry profile at 0.01 mV s^{-1} , between 2.5 – 4.3 V.

Results

Three types of cell were used for electrochemical testing and impedance measurements: (i) a Na/electrolyte/cathode/coin half-cell, Fig. S1, (ii) a three-terminal pouch full-cell, Fig. 1, containing a third, Na electrode placed between the separators, (iii) a two-terminal pouch full-cell similar to (ii) but without the additional Na electrode, Fig. S2. Cycling data for the Na/electrolyte/cathode half-cell (i) between 2.5 and 4.3 V, with a constant voltage hold at the top of charge, are presented in Fig. 2a. After a slightly anomalous first charge attributable to oxygen loss,³¹ the cathode delivered a discharge capacity of around 120 mAh g^{-1} at 14 mA g^{-1} rate across the first 50 cycles. A voltage decay is present in the discharge curves, which may be due to cation migration as reported in the literature for other Li-ion³² and Na-ion cathodes.³³ Cyclic

voltammograms performed at a scan rate of 0.01 mV s^{-1} are shown in (b) for the same cell. A stable trend is observed through cycling, indicating good structural stability of the electrode. Cyclic voltammetry provides information about electrode polarisation curves that are of interest for characterising ageing effects.⁸ However, the response is a composite of all electrochemical processes which complicates the identification of rate-limiting steps.

Two-terminal pouch full-cells (iii) containing the same cathode with a commercially available, hard carbon anode were charged in the 1–4.2 V range using a specific current of 14 mA g^{-1} and discharged at 28 mA g^{-1} . At 4.2 V, a constant voltage hold was used to complete the charging process. Differential capacity plots, Fig. 3a show two spikes on charging, at 3.5 and 4.1 V and two on discharging, at 3.9 and 3.4 V. These features of the dQ/dV curves are

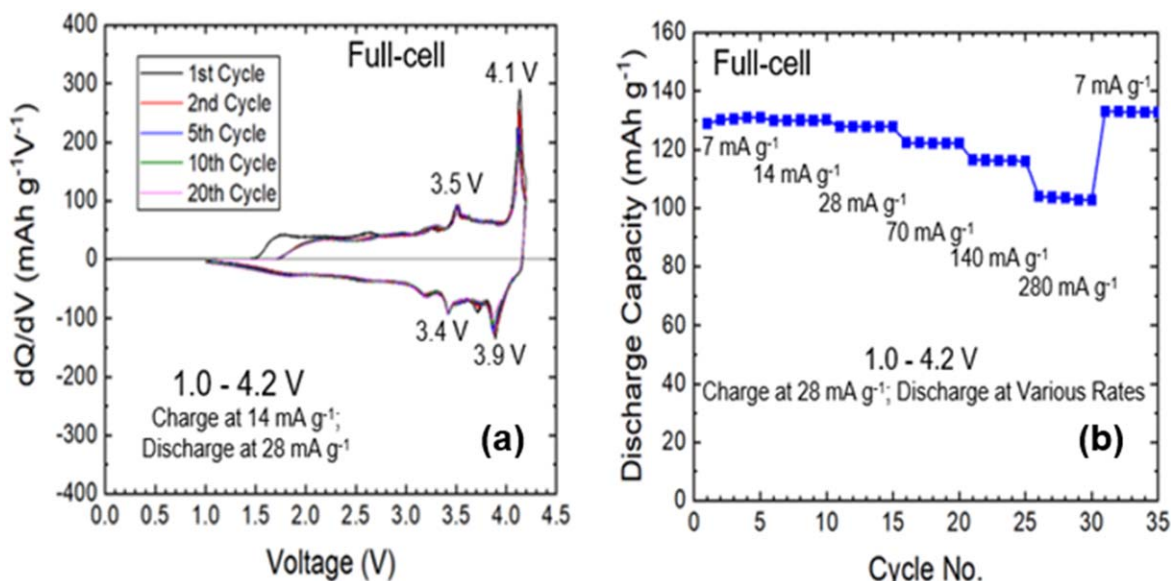


Figure 3. Measurements of Na[Ni,Mg,Mn,Ti]O₂ cathode in full Na-ion cells when paired with commercial hard carbon, showing (a) differential capacity plots of selected cycles and (b) rate performance capabilities.

similar to those observed in the cyclic voltammogram, Fig. 2b with sharp well-defined peaks at high voltage and a profile that is more diffuse at lower voltages.

The discharge rate capability performance of the two-terminal cell is shown in Fig. 3b. The cell exhibited a gradual decline in capacity with increasing discharge current. However, complete recovery was observed when a lower discharge rate of 7 mA g⁻¹ was used subsequently after 30 cycles. In fact, the final capacity was even higher, indicating extra uptake of Na⁺ with cycling, and is a phenomenon reported elsewhere for certain hard carbons.^{31,34,35} These results suggest that the capacity decrease seen at higher discharge rates is due to cell impedance changes, rather than to an irreversible loss of sodium and indicates that cells based on these layered oxide cathodes are suitable candidates for studying performance limitations using EIS.

Figure 4a shows the cell voltage and the individual electrode voltage responses for a three-terminal cell over the first ten cycles. A plot on an expanded scale is provided in Fig. 4b to demonstrate the voltage difference between the full-cell and the cathode. In the fully charged state, the cathode electrode is at ~4.3 V vs Na, while the anode electrode is positioned at around 0.1 V, indicating that the cell is operating under an appropriate cathode/anode charge balance. From the voltage profiles, both electrodes maintain a consistent level of polarization, which is clearly necessary for a long cell cycle life. Further, in the fully charged condition, the negative electrode is comfortably positive of the Na metal potential (0 V vs Na). The excellent stability of the Na reference electrode indicates that this three-electrode cell design is suitable to perform impedance measurements.

The discharge capacities of a standard two-electrode cell undergoing charge-discharge cycling and the three-electrode cell subject to impedance measurements at regular intervals are compared in Fig. 4c. The two plots are very similar indicating that using different cell configurations and simultaneously performing impedance scans and cell cycling, do not affect significantly their cycling performance.

Impedance complex plane plots for the three-electrode cell prior to cycling (ii) are shown in Fig. 5a. The full-cell measurement (black) shows two high frequency semi-circles that do not pass through the origin (see inset). Their intercepts with the Z' axis are ~250 Ω cm at highest frequencies, ~1.5 kΩ cm at ~0.01–1 kHz (inset) and a poorly-resolved intercept of ~25 kΩ cm below ~100 mHz (main diagram). At lowest frequencies, the data give a

steeply-inclined spike. Impedance data for the two-electrode and three-electrode cells across the first ten cycles are compared in Fig. S3. In all cases, the impedance complex plane plots are very similar and indicate that the three-electrode cells are valid for extracting meaningful impedance results of the separate electrode contributions.

Impedance data for the cathode/electrolyte/Na half-cell component of the three-terminal cell are shown in red and closely resemble those of the full-cell at higher frequencies. The only significant difference is that the cathode data do not contain a low-frequency inclined spike. This indicates that the spike is solely associated with the anode and is confirmed by data, shown in blue, for the anode/electrolyte/Na half-cell component. Anode data consist of an almost vertical spike that intercepts the Z' axis near to the origin. The conclusion from these initial results on a fresh cell is that the cathode dominates the cell resistance and the anode dominates its series capacitance.

Figure 5b shows capacitance, C', data extracted from the same impedance data used in (a) and plotted against frequency on logarithmic scales. These also show that the cathode half-cell and full-cell data closely resemble one another over most of the frequency range. Both show a low-frequency plateau around 100 μF cm⁻¹ and a second poorly-defined plateau at ~5 nF cm⁻¹ at higher frequency. At the lowest frequencies, below ~100 mHz, the full-cell C' data begin to increase with decreasing frequency, which is consistent with the appearance of the low frequency, capacitive spike in the anode data (a). The anode capacitance data also show low and intermediate frequency plateaux but their C' values are significantly greater, ~0.5 mF cm⁻¹ and ~50 nF cm⁻¹, apart from at the lowest frequency, 10 mHz, where the C' data for the anode match those of the full-cell.

These data may be represented to a first approximation by the equivalent circuits shown in Fig. 6 for (a) the cathode, (b) the anode and (c) the full-cell. The cathode data show three components, the limiting high frequency resistance R₁ (there will be an associated high frequency parallel capacitance, C₁, giving rise to an additional semicircle, but higher frequency data would be required to access this) and two intermediate frequency elements represented by R₂C₂ and R₃C₃. This circuit, with the addition of constant phase elements, fits accurately impedance data obtained, as shown in Fig. S4.

Initial interpretation of these circuit components is as follows. Resistance R₁ corresponds to the electrolyte resistance, as confirmed by separate measurements (see later). The electrolyte capacitance,

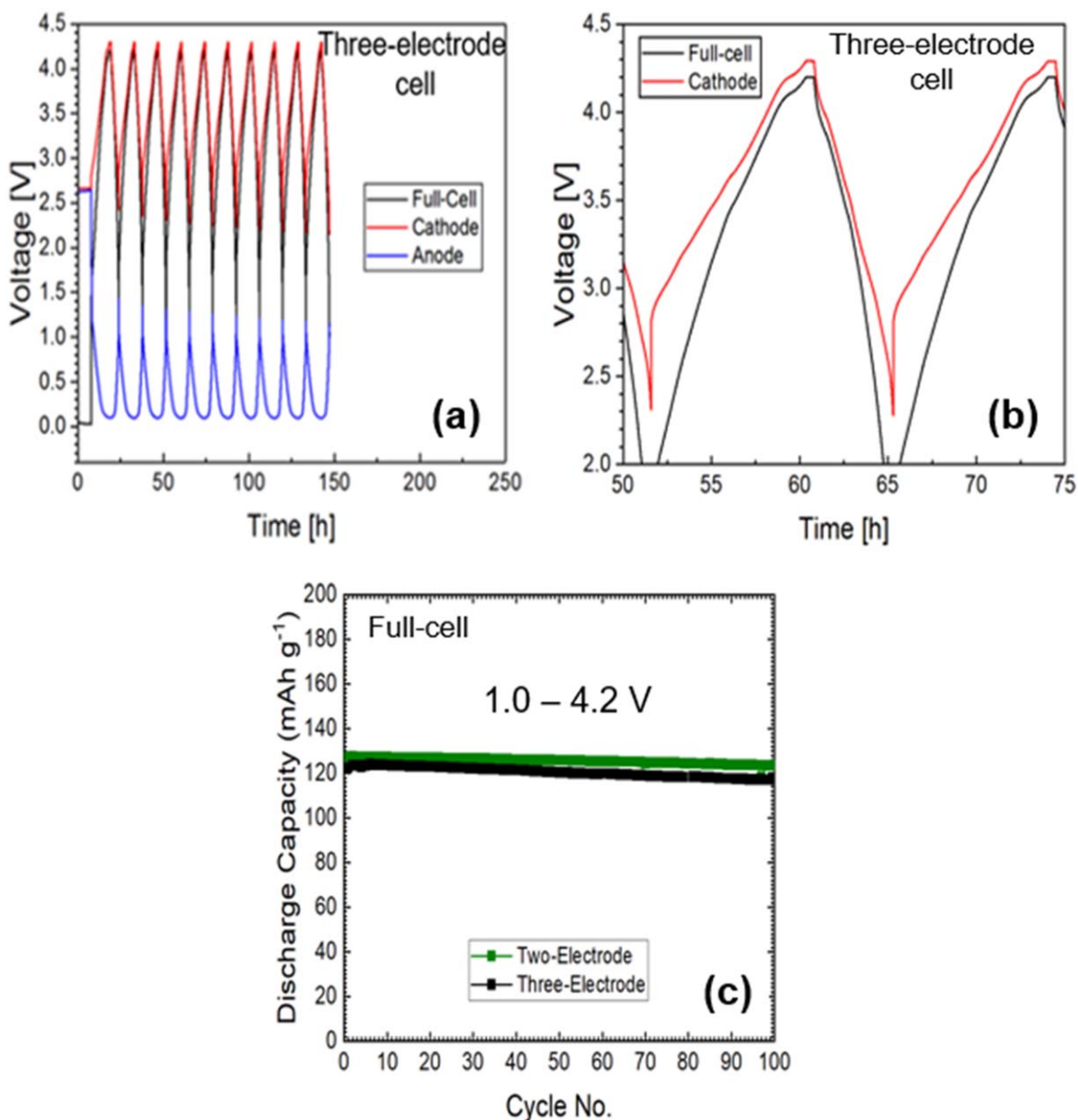


Figure 4. (a) The voltage profile of an in-house, three-electrode Na-ion cell, charged at $C/10$ and discharged at $C/5$ with (b) a zoomed-in view of some of the high voltage data; (c) comparison of discharge capacities for a standard two-electrode cell undergoing normal charge-discharge cycling and a three-electrode cell subject to IS runs at regular intervals.

C_1 , should be in the picoFarad range at high frequencies and is clearly off-scale in Fig. 5b, although the C' data start to decrease significantly above ~ 100 kHz (b). Element R_2C_2 is responsible for the intermediate frequency plateau in C' data; from the magnitude of the capacitance it represents a thin layer resistive component of the cathode. Element R_3C_3 is responsible for the low frequency C' plateau of $50\text{--}120 \mu\text{F cm}^{-2}$. It represents the interface between electrolyte and cathode. If we make the assumption that the Na-electrolyte interface in the cathode half-cell is ohmic, non-blocking and does not contribute significantly to the overall cell impedance, then the cathode-electrolyte interface is essentially capacitive but with a charge transfer resistance, R_{CT} of $25 \text{ k}\Omega$ cm.

The magnitude of the low frequency plateau in the anode half-cell C' data, $\sim 0.5 \text{ mF cm}^{-2}$, is also consistent with a thin layer interfacial effect, but at the carbon/electrolyte interface. The capacitance spike in Fig. 5a does not pass through the origin but gives an intercept in the $50\text{--}100 \Omega$ cm range which, as with cathode data, is attributed to the electrolyte resistance. The presence of the

almost ideal capacitance spike means that it is completely blocking to both ion and electron transport, with the implication that the charge-transfer resistance associated with insertion of Na^+ ions into the carbon is very high in the pristine, un-used cell. The circuit that approximates to the anode data, (a), is therefore a series combination of R_1 and C_4 shown in Fig. 6b. The full-cell is represented by circuit (c).

These results indicate that, prior to first charging of the cell, the cathode-electrolyte interface is partially blocking by a double layer capacitance, C_3 , but with a charge-transfer resistance, R_3 , of $25 \text{ k}\Omega$ cm. Anode half-cell data are capacitive at low frequencies and can be represented ideally by a capacitance that is completely blocking. The presence of a parallel charge-transfer resistance at the anode interface would cause the capacitance spike in Fig. 5a to turn over into an arc at lower frequencies; clearly, this does not happen over the frequency range used and the anode capacitance is completely blocking in the freshly assembled cell. Hence, both electrode-electrolyte interfaces dominate the low frequency impedance data.

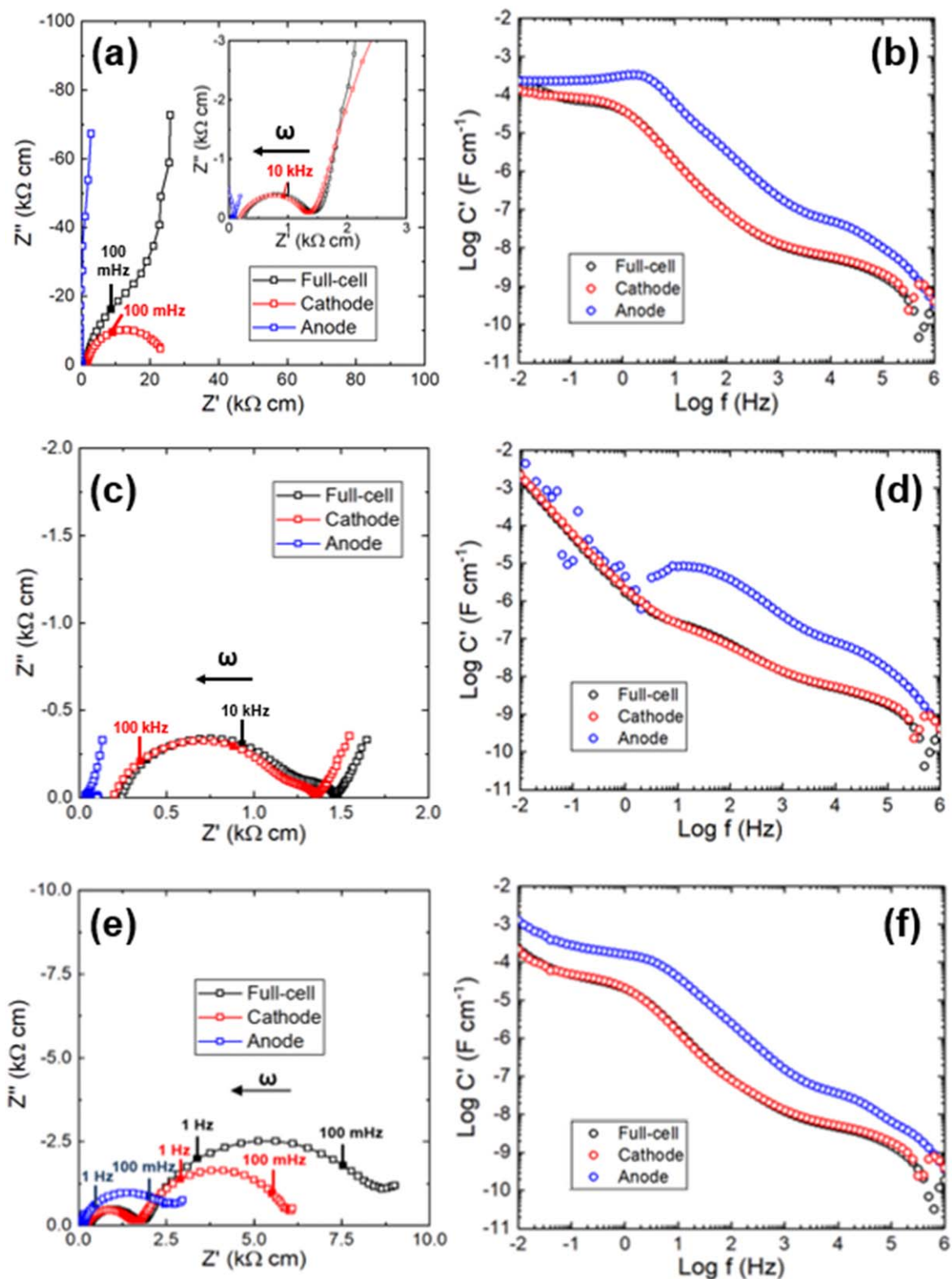


Figure 5. Full-cell, as well as cathode and anode half-cell impedance data for a three-electrode sodium-ion battery. (a) Impedance complex plane plots and (b) spectroscopic plots of C' prior to cycling the cell; (c), (d) after the first charge; (e), (f) after first discharge.

The anode interface represents the difficulty of insertion of Na^+ ions into the carbon anode, if it is assumed that the current collector—carbon electrode contact is ohmic. The cathode interface has a large resistance associated presumably with transfer of Na^+ ions between cathode and electrolyte although in this case, electron transfer

between the Al current collector and the oxide cathode may have a significant impedance.

Impedance data for the same three-electrode cell after first charge and discharge cycles are shown in Figs. 5c–5f. The high frequency resistive components of the two half-cell and full-cell impedances

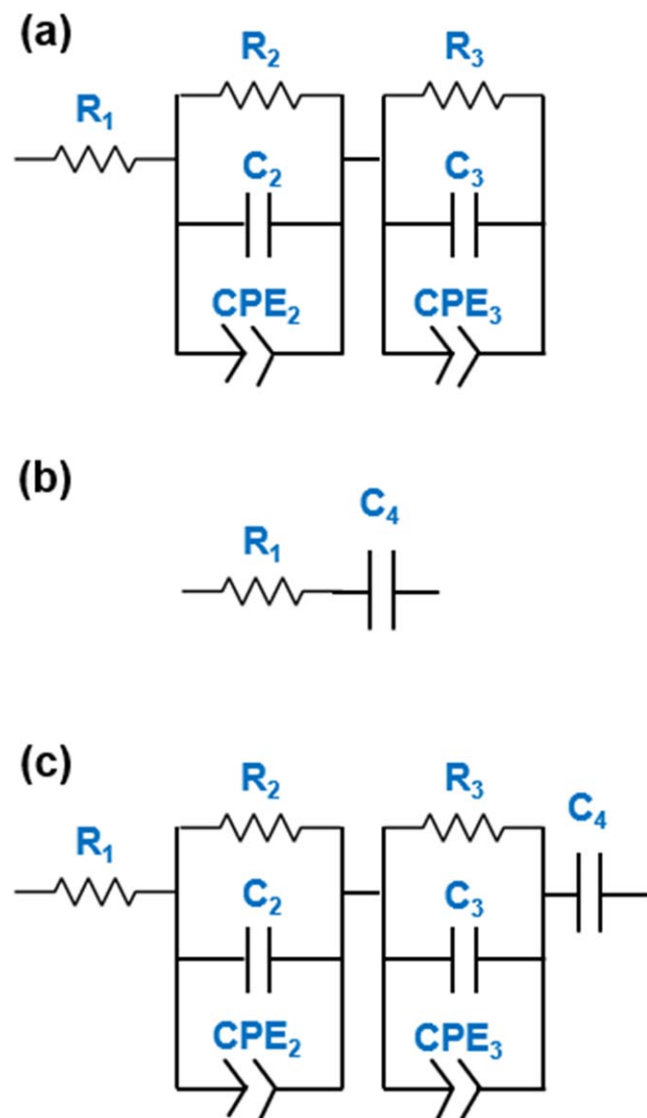


Figure 6. Equivalent electrical circuits for (a) cathode, (b) anode and (c) full-cell data, for a three-electrode sodium-ion battery prior to cycling.

are similar after and before the first charge, (a,c) with intercepts representing R_1 and R_2 on the Z' axis; values of R_1 are in the range $100\text{--}200\ \Omega\ \text{cm}$ and R_2 $1.3\text{--}1.5\ \text{k}\ \Omega\ \text{cm}$. Assignment of R_1 to the electrolyte was confirmed by measurements of a cell consisting of the sodium electrolyte alone in contact with Pt electrodes, Fig. S5. The data, Fig. 7, show a blocking capacitance spike with intercept on the Z' axis of $170\ \Omega\ \text{cm}$. The spike comes from a large charge-transfer resistance at the Pt / Na electrolyte interface. The bulk capacitance of the electrolyte would give rise to a semi-circle at higher frequency than measured and therefore, cannot be seen in Fig. 7. R_1 is shown in each circuit in Fig. 6 as the electrolyte resistance was present in every measurement: cathode, anode and full-cell.

The low frequency impedances are significantly different after the first charge, Figs. 5c–5f. First, the low frequency resistance R_3 has almost disappeared from the cathode half-cell and full-cell impedances (c). Second, the low frequency C' data no longer show the blocking capacitance plateau, C_3 , at $50\text{--}120\ \mu\text{F}\ \text{cm}^{-1}$; instead, C' increases systematically to $> 1\ \text{mF}\ \text{cm}^{-1}$ at lowest frequencies, consistent with electrochemical reaction at the cathode and Na^+ ion transfer across the cathode-electrolyte interface (d). Third, the capacitance of the anode half-cell no longer shows completely blocking behaviour.

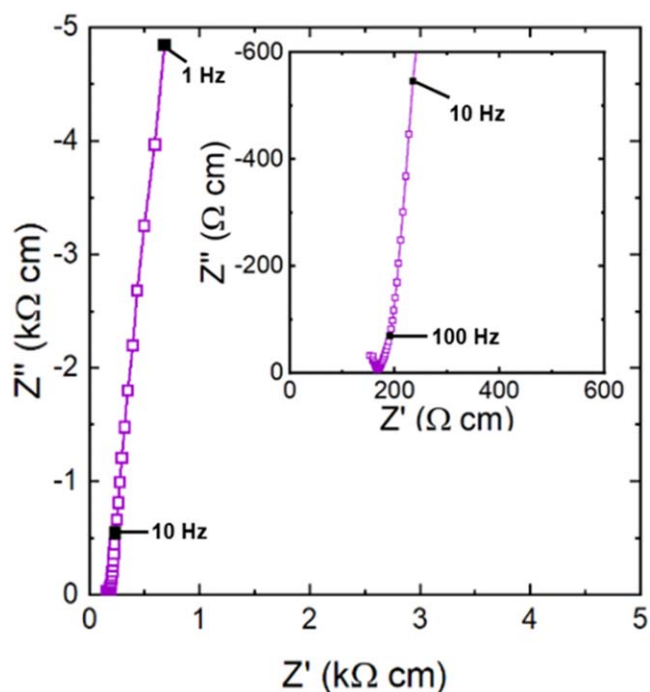


Figure 7. Impedance complex plane plot for the sodium electrolyte. Inset shows expanded high-frequency data.

Impedance data after the first discharge, (e), (f) show significant increases in resistance at low frequencies for both half-cells and the full-cell. First, component R_3C_3 reappears in the cathode half-cell data but with $R_3 \sim 4.5\ \text{k}\ \Omega\ \text{cm}$, which is less than in the fresh cell, $\sim 25\ \text{k}\ \Omega\ \text{cm}$. Second, a new component appears in the anode half-cell data with resistance $\sim 3\ \text{k}\ \Omega\ \text{cm}$ and capacitance $\sim 200\ \mu\text{F}\ \text{cm}^{-1}$. Both interfaces now show typical characteristics of partially blocking behaviour with significant charge-transfer resistances. Impedance measurements were then carried out on cells subjected to a further ten charge–discharge cycles, Fig. 8. The general shapes of the impedance responses were as seen after the first cycle, Fig. 5; the cathode and full-cell resistances increased gradually in both the charged and discharged states (a), (b). Changes to the anode resistances were smaller and appeared to increase after the charging cycles but decrease after the discharging cycles.

Discussion

Use of three-terminal cells enables the separation of anode and cathode contributions to overall cell impedances. Comparison between two- and three-electrode results show that the different cell designs are comparable in terms of capacities and IS results. In this way, cells can be examined, in situ, prior to use and at various points during charge-discharge cycles. A geometry correction was used to convert impedance data to resistivity ($\Omega\ \text{cm}$) and permittivity ($\text{F}\ \text{cm}^{-1}$) units, which would allow comparison of results obtained in this work to data obtained on cells of different capacity and size.

Impedance complex plane presentations of data highlight the largest resistances in datasets. Conversion of impedance data to the permittivity formalism allows separation of impedance components according to capacitance values. Since the impedance components of a battery are series-connected, assignment of their capacitances to different regions can be made since their magnitudes depend directly on thickness of the region responsible.

Impedance data on a prototype Na-ion battery constructed from hard carbon anode, sodium hexafluorophosphate-based liquid electrolyte and layered rock salt cathode are reported for a pristine cell and at various stages of charge-discharge cycles. Results indicate that the anode interface is mainly responsible for the impedance

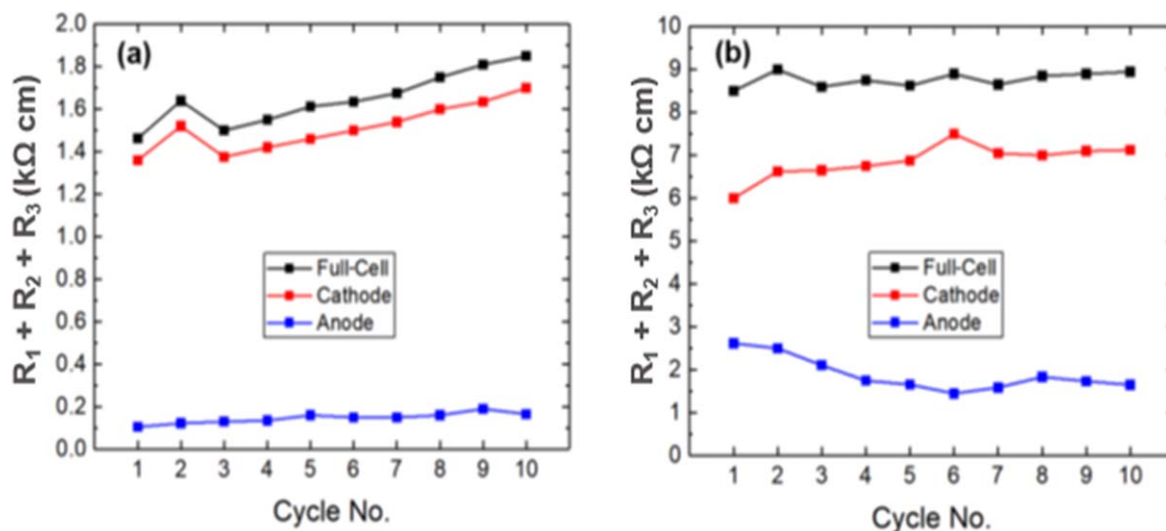


Figure 8. The resistances inside a three-electrode cell (a) after charge and (b) after discharge, across the first 10 cycles.

prior to cycling. This reduced dramatically on first charging of the cell, and the cathode then dominated the overall resistance. The cathode resistance grew during the first ten cycles. Modelling the response using an ideal equivalent circuit found that the cathode impedance consists of three resistive components: a small high-frequency non-zero intercept resistance, R_1 , and two RC elements, with resistances of R_2 and R_3 , at medium and low frequencies respectively.

In the pristine cell, the carbon-electrolyte interface was completely blocking to Na^+ ion transfer across the interface whereas the electrolyte-cathode interface was only partially blocking but with a large charge-transfer resistance of $\sim 25 \text{ k}\Omega \text{ cm}$. There is not much change in the impedance response at high frequency on the first cycle of the cell, but there was a significant change at low frequency. After the first charge cycle, the blocking nature of the cathode interface disappeared completely and instead, showed redox behaviour with capacitances rising through the milliFarad range at low frequencies that could be linked to a low frequency Warburg impedance. The cathode interface also developed a small charge-transfer resistance, $\sim 4.5 \text{ k}\Omega \text{ cm}$, in the discharged state that was smaller than in the pristine cell but larger than that in the charged cell. The blocking nature of the anode interface decreased during the first charge but a new impedance of value $\sim 2.5 \text{ k}\Omega \text{ cm}$ developed after discharge, when the cell was at an OCV of 1.8 V. OCV measurements are dependent upon the different degradation modes occurring inside the battery, and by developing a suitable model and diagnostic algorithm, may also be used to extract important cell parameters, such as state of health.³⁶ However, OCV readings provide information only on degradation of the cell thermodynamics and not kinetic data that can be obtained by IS.

The anodic resistance decreased across the first few cycles, which may be attributed to formation of a stable solid electrolyte interphase. SEI layers are believed to form initially during the first cycle, but their chemical composition and associated resistance may continue to alter during the first few successive charge/discharge reactions.³⁷ There may also be a difference in SEIs in lithium- and sodium-ion batteries, as reported in the literature.³⁵ The SEI layer in Na-ion batteries is not well understood³⁴ and further work may be required to account for the anodic impedances measured in this study.

In addition to the two interfacial impedances which together dominated the overall cell resistance, an additional cathode impedance was present whose resistance changed little during the various impedance measurements. Its associated capacitance of value $\sim 1\text{--}10 \text{ nF cm}^{-1}$ was intermediate between those expected for a sample bulk, $\sim 1\text{--}10 \text{ pF cm}^{-1}$

or grain boundary, $\sim 0.1\text{--}1.0 \text{ nF cm}^{-1}$ and a sample-electrode interface, $\sim 1\text{--}10 \mu\text{F cm}^{-1}$. Possibly, it represents a surface layer of different structure/composition on the cathode particles or a depletion/accumulation layer on one side of the sample-electrode interface. We note the presence of a similar capacitance, $10\text{--}100 \text{ nF cm}^{-1}$, in the anode data.

Evaluating ageing mechanisms in batteries is a difficult topic and involves techniques that vary in complexity and accuracy for separating contributing causes. Previous work has studied the anode interface in Na-ion batteries,³⁸ but the cathode interface is less well studied and understood. Most techniques for probing cathode-electrolyte interface, such as NMR, XPS and EELS operate under ex situ or non-operando conditions,³⁹ unlike in situ IS performed in this work. Post-mortem studies,⁴⁰ where the cell is disassembled and studied, may not preserve the various parts of the cell “intact,” without contamination of the materials to be studied and sample preparation prior to performing certain measurements such as SEM/TEM, may introduce artefacts into the results. Furthermore, destructive testing eradicates the ability to gather information on dynamic processes that occur during battery operation, therefore curtailing its usefulness. Techniques capable of performing in situ measurements usually require custom built cells,⁴¹ which may introduce features that affect the electrochemical performance, and hence, impact degradation processes. Identifying interfacial chemical species and quantifying their evolution under in situ/operando conditions require a range of complementary techniques with both high specificity and high sensitivity that can complement the direct impedance results obtained from IS measurements and is an area of future work.

Conclusions

These studies and preliminary conclusions show the potential of impedance measurements on three-terminal cells to provide novel, direct insights into cell impedances and the factors that contribute to cell performance. Cells can be monitored in situ from their initial assembly to various points in successive charge-discharge cycles.

The impedance of pristine un-used cells is dominated by combination of a blocking capacitance at the anode-electrolyte interface and a large transfer resistance at the cathode-electrolyte interface. On cycling, both of these impedances diminish in importance but new impedances appear which, from the magnitudes of their capacitances in the $1\text{--}10 \text{ nF}$ range, appear to be associated with thin layer effects at the electrode-electrolyte interfaces. The nature of an SEI at the anode interface has been discussed in the literature but the possibility of a similar SEI, or alternative layer, at the cathode interface or surface requires further study.

Acknowledgments

We thank the EPSRC under grant EP/L016818/1 for a PhD studentship for L. Middlemiss.

ORCID

Laurence A. Middlemiss  <https://orcid.org/0000-0002-7840-4393>
 Anthony R. West  <https://orcid.org/0000-0002-5492-2102>

References

- D. Deng, *Energy Sci. Eng.*, **3**, 385 (2015).
- J. Y. Hwang, S. T. Myung, and Y. K. Sun, *Chem. Soc. Rev.*, **46**, 3529 (2017).
- J. B. Robinson, D. P. Finegan, T. M. M. Heenan, K. Smith, E. Kendrick, D. J. L. Brett, and P. R. Shearing, *J. Electrochem. En. Conv. Stor.*, **15**, 1 (2018).
- S. W. Kim, D. H. Seo, X. Ma, G. Ceder, and K. Kang, *Adv. Energy Mater.*, **2**, 710 (2012).
- M. Broussely, P. Biensan, F. Bonhomme, S. Herreyre, K. Nechev, and R. J. Staniewicz, *J. Power Sources*, **146**, 90 (2005).
- R. B. Wright, J. P. Christophersen, C. G. Motloch, J. R. Belt, C. D. Ho, V. S. Battaglia, J. A. Barnes, T. Q. Duong, and R. A. Sutula, *J. Power Sources*, **119**, 865 (2003).
- J. Vetter, P. Novák, M. R. Wagner, C. Veit, K.-C. Moller, J. O. Besenhard, M. Winter, M. Wohlfahrt-Mehrens, C. Vogler, and A. Hammouche, *J. Power Sources*, **147**, 269 (2005).
- U. Tröltzsch, O. Kanoun, and H.-R. Tränkler, *Electrochim. Acta*, **51**, 1664 (2006).
- T. Osaka, T. Momma, D. Mukoyama, and H. Nara, *J. Power Sources*, **205**, 483 (2012).
- F. Huet, *J. Power Sources*, **70**, 59 (1998).
- M. Itagaki, K. Honda, Y. Hoshi, and I. Shitanda, *J. Electroanal. Chem.*, **737**, 78 (2015).
- L. Wang, J. Zhao, X. He, J. Gao, J. Li, C. Wan, and C. Jiang, *Int. J. Electrochem. Sci.*, **7**, 345 (2012).
- J. Y. Song, H. H. Lee, Y. Y. Wang, and C. C. Wan, *J. Power Sources*, **111**, 255 (2002).
- C. H. Chen, J. Liu, and K. Amine, *J. Power Sources*, **96**, 321 (2001).
- T. Momma, T. Yokoshima, H. Nara, Y. Gima, and T. Osaka, *Electrochim. Acta*, **131**, 195 (2014).
- G. Nagasubramanian, *J. Power Sources*, **87**, 226 (2000).
- I. J. Gordon, S. Genies, G. Si Larbi, A. Boulineau, L. Daniel, and M. Alias, *J. Power Sources*, **307**, 788 (2016).
- S. P. Rangarajan, S. Sarkar, Y. Barsukov, and P. P. Mukherjee, *ACS Omega*, **6**, 33284 (2021).
- G. Nagasubramanian, *J. Appl. Electrochem.*, **31**, 99 (2001).
- M.-S. Wu, P.-C. J. Chiang, and J.-C. Lin, *J. Electrochem. Soc.*, **152**, A47 (2004).
- E. McTurk, C. R. Birkl, M. R. Roberts, D. A. Howey, and P. G. Bruce, *ECSS Electrochem. Lett.*, **4**, A145 (2015).
- C. Bünzli, H. Kaiser, and P. Novák, *J. Electrochem. Soc.*, **162**, A218 (2015).
- S. Klink, D. Höche, F. La Mantia, and W. Schuhmann, *J. Power Sources*, **240**, 273 (2013).
- G. Hsieh, S. J. Ford, T. O. Masona, and L. R. Pederson, *Solid State Ion.*, **91**, 192 (1996).
- I. M. Hodge, M. D. Ingram, and A. R. West, *J. Electroanal. Chem. Interfacial Electrochem.*, **74**, 125 (1976).
- J. T. S. Irvine, D. C. Sinclair, and A. R. West, *Adv. Mater.*, **2**, 132 (1990).
- D. Andre, M. Meiler, K. Steiner, C. Wimmer, T. Soczka-Guth, and D. U. Sauer, *J. Power Sources*, **196**, 5334 (2011).
- D. Andre, M. Meiler, K. Steiner, H. Walz, T. Soczka-Guth, and D. U. Sauer, *J. Power Sources*, **196**, 5349 (2011).
- D. Zhang, B. S. Haran, A. Durairajan, R. E. White, Y. Podrazhansky, and B. N. Popov, *J. Power Sources*, **91**, 122 (2000).
- L. A. Middlemiss, A. J. R. Rennie, R. Sayers, and A. R. West, *Energy Rep.*, **6**, 232 (2020).
- A. Rudola, A. J. Rennie, R. Heap, S. S. Meysami, A. Lowbridge, F. Mazzali, R. Sayers, C. J. Wright, and J. Barker, *J. Mater. Chem. A*, **9**, 8279 (2021).
- M. Sathiyaraj et al., *Nat. Mater.*, **14**, 230 (2015).
- S. Xu et al., *J. Mater. Chem. A*, **6**, 20795 (2018).
- Y. Pan, Y. Zhang, B. S. Parimalan, C. C. Nguyen, G. Wang, and B. L. Lucht, *J. Electroanal. Chem.*, **799**, 181 (2017).
- R. Mogensen, D. Brandell, and R. Younesi, *ACS Energy Lett.*, **1**, 1173 (2016).
- C. R. Birkl, M. R. Roberts, E. McTurk, P. G. Bruce, and D. A. Howey, *J. Power Sources*, **341**, 373 (2017).
- P. Verma, P. Maire, and P. Novák, *Electrochim. Acta*, **55**, 6332 (2010).
- S. Sarkar and P. P. Mukherjee, *Energy Storage Mater.*, **43**, 305 (2021).
- M. Linqin et al., *Adv. Energy Mater.*, **8**, 1801975 (2018).
- T. Waldmann et al., *J. Electrochem. Soc.*, **163**, 2149 (2016).
- D. Chen, M. A. Mahmoud, J.-H. Wang, G. H. Waller, B. Zhao, C. Qu, M. A. El-Sayed, and M. Liu, *Nano Lett.*, **19**, 2037 (2019).